Coupling of a global MHD code and an inner magnetospheric model: Initial results

Darren L. De Zeeuw

Center for Space Environment Modeling, University of Michigan, Ann Arbor, Michigan, USA

Stanislav Sazykin and Richard A. Wolf

Department of Physics and Astronomy, Rice University, Houston, Texas, USA

Tamas I. Gombosi, Aaron J. Ridley, and Gabor Tóth

Center for Space Environment Modeling, University of Michigan, Ann Arbor, Michigan, USA

[1]   This paper describes the coupling of BATS-R-US (Block Adaptive Tree Solar-wind Roe-type Upwind Scheme), a magnetohydrodynamics (MHD) code representing the Earth's global magnetosphere and its coupling to the ionosphere and solar wind, and the Rice Convection Model (RCM), which represents the inner magnetosphere and its coupling to the ionosphere. The MHD code provides a time-evolving magnetic field model for the RCM as well as continuously updated boundary conditions for the electric potential and plasma. The RCM computes the distribution functions of inner magnetospheric particles, including transport of inner plasmasheet and ring current particles by gradient/curvature drifts; it thus calculates more accurate inner magnetospheric pressures, which are frequently passed to the MHD model and used to nudge the MHD values. Results are presented for an initial run with the coupled code for the case of uniform ionospheric conductance with steady solar wind and southward interplanetary magnetic field (IMF). The results are compared with those for a run of the MHD code alone. The coupled-code run shows significantly higher inner magnetospheric particle pressures. It also exhibits several well-established characteristics of inner magnetospheric electrodynamics, including strong region-2 Birkeland currents and partial shielding of the inner magnetosphere from the main force of the convection electric field. A sudden northward turning of the IMF causes the ring current to become more nearly symmetric. The inner magnetosphere exhibits an overshielding (dusk-to-dawn) electric field that begins about 10 min after the northward turning reaches the magnetopause and lasts just over an hour.   *INDEX TERMS:* 2730 Magnetospheric Physics: Magnetosphere—inner; 2753 Magnetospheric Physics: Numerical modeling; 2778 Magnetospheric Physics: Ring current; 2708 Magnetospheric Physics: Current systems (2409); *KEYWORDS:* magnetohydrodynamics, space weather, model coupling, global magnetosphere, inner magnetosphere

1.   Introduction

[2]   From the viewpoint of large-scale theoretical modeling, the Earth's magnetosphere is divided into two parts. The inner part includes all field lines that extend to geocentric distances less than $\sim 8\ R_E$ in the equatorial plane. The outer magnetosphere may be reasonably described by single-fluid magnetohydrodynamics (MHD), which is capable of spanning the huge region (hundreds of thousands of R_E^3) computationally. Small-scale, non-MHD plasma processes play an important role in the dynamics of the region, notably by magnetic reconnection and auroral particle

acceleration, but these occur in limited regions. Though other techniques are being developed [e.g., *Nishikawa*, 2001; *Delamere et al.*, 2001], global MHD codes represent the state-of-the-art in theoretical representation of the outer magnetosphere [e.g., *Ogino and Walker*, 1984; *Lyon et al.*, 1986; *Winglee*, 1994; *Raeder et al.*, 1995; *Tanaka*, 1995; *Janhunen*, 1996; *White et al.*, 1998; *Powell et al.*, 1999].

[3]   Standard single-fluid MHD cannot provide adequate description of the inner magnetosphere, however, because the main pressure-bearing particles in that region are the $1-200$ keV ions of the inner plasma sheet and ring current. For these particles, $\mathbf{E} \times \mathbf{B}$ drift, which provides all cross-$\mathbf{B}$ transport in ideal MHD, is often slower than gradient and curvature drift. In fact, since the gradient/

curvature drift speed is proportional to particle energy, there is little hope that any single-fluid representation can describe inner-magnetospheric particle transport with reasonable accuracy.

[4] Theoretical models treating the main pressure-bearing particles of the inner magnetosphere, which typically keep separate account of tens or hundreds of components of the plasma, have traditionally fallen in two categories: "ring current models" and "convection models." Traditional ring current models follow particles with different values of the first and second adiabatic invariants and calculate energy and pitch angle distributions in some detail, carefully considering loss by charge exchange and precipitation. These ring current models [e.g., *Chen et al.*, 2000; *Liemohn et al.*, 2002; *Fok et al.*, 1999; *Jordanova et al.*, 2001] take the electric and magnetic fields as input models rather than computing them self-consistently. Convection models [e.g., *Peymirat et al.*, 2002; *Sazykin et al.*, 2002; *Ridley and Liemohn*, 2002] calculate inner magnetospheric electric fields self-consistently with the particles but use input magnetic fields that are not calculated self-consistently. These convection models generally assume an isotropic pitch angle distribution, do not treat H^+ and O^+ separately, and either neglect loss or calculate it in less detail than the ring current models.

[5] In recent years, some attempts have been made at inner magnetosphere models that are more comprehensive and self-consistent. *Fok et al.* [2001] combined the Rice Convection Model with a ring current model, calculating potential electric fields self-consistently and computing pitch angle distributions and charge exchange loss in detail. *Toffoletto et al.* [1996, 2000, 2001] coupled a friction code equilibrium solver to the Rice Convection Model to compute the magnetic fields self-consistently with the particle distribution, within the assumption of isotropic pitch angles; much of the magnetotail is formally included in the modeling region, but this model cannot represent the physics of reconnection, and it uses arbitrary conditions on the tail boundaries rather than representing solar wind/magnetosphere interactions. Until now, there has been no model that self-consistently represent the solar wind driven magnetosphere with accurate particle treatment.

[6] There are strong reasons for developing models that physically couple the inner and outer magnetospheres. For one thing, the magnetospheric substorm, a central dynamic process of the magnetosphere, is centered near the boundary between the inner and outer magnetospheres. Magnetic storms involve coupled changes in both the inner and outer magnetosphere. Even some processes that seem to be clearly in the inner or outer magnetosphere actually turn out to involve both regions. For example, ring current inflation of the inner magnetospheric magnetic field significantly affects magnetic field mapping between ionosphere and the tail [*Siscoe*, 1979]. *Siscoe et al.* [2002] have suggested that polar cap potential drop depends on inner magnetospheric region-2 Birkeland currents. The penetration of the magnetospheric electric field to the innermost part of the magnetosphere and the equatorial ionosphere depends on the magnetic flux in the tail [*Fejer et al.*, 1990]. The overall conclusion is that it is not possible to treat the inner magnetosphere accurately without an accurate representation of the outer magnetosphere, and vice versa.

[7] This paper reports a successful effort to join a global MHD model, the Block Adaptive Tree Solar-wind Roe-type Upwind Scheme (BATS-R-US), with the Rice Convection Model (RCM). The MHD model, which has its inner boundary at 2.5 R_E, provides the RCM with values for the potential and plasma bulk parameters at the RCM outer boundary, defined by field lines that have equatorial crossing points on an ellipse that extends to approximately 8 R_E at local noon, 7 R_E at dawn and dusk, and 10 R_E at midnight (the exact boundary location changes due to the evolution of the open/closed field region boundary). The MHD code also provides the RCM with an initial pressure and density distribution. More importantly, MHD calculates the magnetic field inside the RCM's modeling region. The RCM provides corrected pressure values for the inner magnetosphere, which are used to nudge the MHD values.

[8] Coupling these two models was a substantial computational challenge because the two codes speak different languages. MHD employs a fluid formalism and works on a three-dimensional (3-D) grid. The RCM treats its particles with an adiabatic particle drift formalism, treats each flux tube as a unit, and uses a 2-D grid. A major computational challenge lay in efficient exchange of information between the two codes because every exchange requires tracing a very large number of field lines.

2. Description of BATS-R-US

[9] The Block-Adaptive-Tree Solar-wind Roe-type Upwind Scheme (BATS-R-US) code solves the governing equations of magnetohydrodynamics. All terms describing deviations from ideal MHD are included through appropriate source terms. An overview of BATS-R-US can be found in Appendix A. A more detailed description of the code can be found in the work of *Powell et al.* [1999] and in the work of *De Zeeuw et al.* [2000].

[10] The governing equations for an ideal, nonrelativistic, compressible plasma may be written in a number of different forms. In primitive variables, the governing equations, which represent a combination of the Euler equations of gasdynamics and the Maxwell equations of electromagnetics, may be written as

$$\frac{\partial \rho}{\partial t} + \mathbf{u} \cdot \boldsymbol{\nabla}\rho + \rho\boldsymbol{\nabla} \cdot \mathbf{u} = 0$$
$$\rho\frac{\partial \mathbf{u}}{\partial t} + \rho\mathbf{u} \cdot \boldsymbol{\nabla}\mathbf{u} + \boldsymbol{\nabla}p - \mathbf{j} \times \mathbf{B} = 0$$
$$\frac{\partial \mathbf{B}}{\partial t} + \boldsymbol{\nabla} \times \mathbf{E} = 0 \tag{1}$$
$$\frac{\partial p}{\partial t} + \mathbf{u} \cdot \boldsymbol{\nabla}p + \gamma p\boldsymbol{\nabla} \cdot \mathbf{u} = 0,$$

where the current density $\mathbf{j}$ and the electric field vector $\mathbf{E}$ are related to the magnetic field $\mathbf{B}$ by *Ampère's law* and *Ohm's law*, respectively:

$$\mathbf{j} = \frac{1}{\mu_0}\boldsymbol{\nabla} \times \mathbf{B}$$
$$\mathbf{E} = -\mathbf{u} \times \mathbf{B}. \tag{2}$$

BATS-R-US solves the MHD equations with a finite volume discretization using the conservative variables: density ρ, momentum density $\rho\mathbf{u}$, magnetic field $\mathbf{B}$, and

the total energy density e, which is the sum of the thermal, kinetic, and magnetic energy densities.

[11] The state of the magnetosphere is controlled by conditions in the solar wind and in the ionosphere. Solar wind conditions are imposed as boundary conditions at the upwind boundary of the simulation domain.

3. Description of the RCM

[12] The Rice Convection Model (RCM), a large numerical computer code developed over 30 years at Rice University, offers a self-consistent description of the electrodynamics of the coupled inner magnetosphere-ionosphere system. The code solves the time-dependent coupled equations of plasma motion in the magnetosphere and of conservation of current in the ionosphere. Descriptions of the algorithms and numerical details have been provided by *Harel et al.* [1981a], *Sazykin* [2000], and *Toffoletto et al.* [2003].

[13] The RCM modeling region in the magnetosphere typically extends from just inside the magnetopause on the dayside of Earth to the middle plasma sheet ($\approx 25\ R_E$) on the nightside. In this region, which is characterized by closed magnetic field lines, the plasma is assumed to undergo slow flow [*Wolf*, 1983]. The model represents the particle distribution function by a number (typically on the order of 100) of isotropic "fluids." Each fluid is characterized by an energy invariant λ_s, flux tube content η_s and charge q_s, which are related to the kinetic energy W_s and number density n_s through the flux tube volume $V = \int ds/B$:

$$\lambda_s = W_s V^{2/3} \qquad \eta_s = n_s V \qquad (3)$$

(index s specifies a given energy invariant and chemical species). Under these approximations, the RCM advects each fluid using

$$\frac{\partial \eta_s}{\partial t} + \frac{\mathbf{B} \times \boldsymbol{\nabla}\left(\Phi + \Phi_c + \frac{\lambda_s}{q_s} V^{-2/3}\right)}{B^2} \cdot \nabla \eta_s = -L. \qquad (4)$$

Φ is the electric potential in the ionosphere where the induction electric field is negligible, expressed in a coordinate system that rotates with the planet; Φ_c is the corotation potential, which converts the potential to a frame that does not rotate with the Earth; the symbol L represents explicit losses (typically due to charge exchange and precipitation; outflow through the dayside magnetopause is implicit in the RCM solution of the advection equations). The *Vasyliunas* [1970] equation is used to calculate the field-aligned current:

$$J_{\|i} = \frac{1}{2}\hat{b} \cdot \boldsymbol{\nabla} V \times \boldsymbol{\nabla} P, \qquad (5)$$

where $J_{\|i}$ is the current density into the northern ionosphere, $\hat{b}$ is a unit magnetic field vector, and the right side is evaluated at the ionosphere. The pressure P is given by $(2/3)V^{-5/3}\Sigma_s \lambda_s \eta_s$. The factor of 1/2 comes from the assumption of symmetry between northern and southern ionospheres. The potential distribution is computed from the condition for current conservation at the ionosphere:

$$\boldsymbol{\nabla} \cdot \left[-\overleftrightarrow{\Sigma} \cdot \nabla \Phi + \mathbf{j}_w\right] = J_{\|i}\sin(I), \qquad (6)$$

where the operator $\boldsymbol{\nabla}$ acts on the two-dimensional ionospheric spherical shell, $\overleftrightarrow{\Sigma}$ is a 2×2 conductance tensor, and I is the dip angle of the magnetic field below the horizontal plane. The $\mathbf{j}_w$ term represents ionospheric current driven by neutral winds and involves field line integrals of products of wind velocities and conductances. The elements of the conductance tensor are expressed through the field line integrals of Pedersen (σ_P) and Hall (σ_H) conductivities with integration extending from the bottom (90 km) to the top (1000 km) of the ionosphere:

$$\overleftrightarrow{\Sigma} = \begin{pmatrix} \Sigma_{\theta\theta} & \Sigma_{\theta\phi} \\ -\Sigma_{\theta\phi} & \Sigma_{\phi\phi} \end{pmatrix}, \qquad (7)$$

where $\Sigma_{\theta\theta} = \int ds\ \sigma_P/\sin I$, $\Sigma_{\phi\phi} = \sin I \int ds\ \sigma_P$, $\Sigma_{\theta\phi} = -\Sigma_{\phi\theta} = \int ds\ \sigma_H$. The components of $\mathbf{j}_w$ can be similarly expressed in terms of field line integrals.
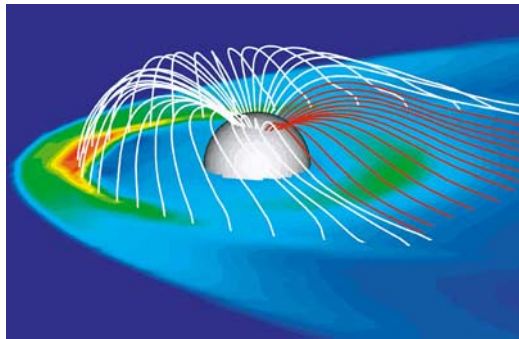
[14] The boundary conditions for the particle density in (4) are usually taken from statistical plasma sheet models or from data from a geosynchronous particle detector if the boundary is set at $L = 6.6$ [*Sazykin et al.*, 2002]. Given initial conditions, (4) is integrated in time with a short time step (typically 1 to 5 s). Updated solutions to (4) are used to compute the updated particle pressure distribution, which provides the right-hand side of the elliptical equation (6), using (5). Equation (6) is solved everywhere in the ionosphere from near the equator ($L = 1.03$) to the poleward boundary. The magnitude of the electric potential on the poleward boundary is controlled by solar wind conditions.

[15] For most RCM runs, the conductance $\overleftrightarrow{\Sigma}$ is computed from an IRI-90 ionospheric model and auroral enhancement computed assuming 30% of the strong pitch angle scattering limit and using the *Robinson et al.* [1987] formula to calculate conductances; field-aligned potential drops are usually neglected. However, for these first runs in which the RCM is coupled to MHD, both codes assume simply zero Hall conductance and a uniform Pedersen conductance of 4 S in each hemisphere. Neutral winds are set to zero for the present run, as are field-aligned potential drops.

[16] The RCM's treatment of the equatorial electrojet follows the approach of *Blanc and Richmond* [1980] using the thin-band approximation, in which the zonal electric field is assumed independent of latitude in the band and the meridional current is assumed to be much less intense than the zonal current. The new potential found from (6) is used to advance the advection equations (4), closing the logical loop. The RCM thus steps along in time, self-consistently calculating the particle distribution and electric fields and currents, driven by several inputs: the magnetic field configuration and the potential drop and inflowing particle fluxes on the high-latitude boundary.

[17] The RCM has successfully been used to explicate major magnetospheric phenomena such as the development of region-2 Birkeland currents which shield the magnetosphere [e.g., *Jaggi and Wolf*, 1973; *Harel et al.*, 1981b], the buildup and evolution of the storm-time ring current [e.g., *Wolf et al.*, 1982; *Spiro and Wolf*, 1984; *Sazykin et al.*, 2002; *Fok et al.*, 2003; *Garner*, 2003], formation and evolution of the plasmasphere and plasmapause [e.g., *Spiro et al.*, 1981; *Wolf et al.*, 1986], the penetration of convection electric fields to low ionospheric latitudes [e.g., *Spiro et al.*, 1988; *Fejer et al.*, 1990; *Sazykin*, 2000], the Harang discontinuity
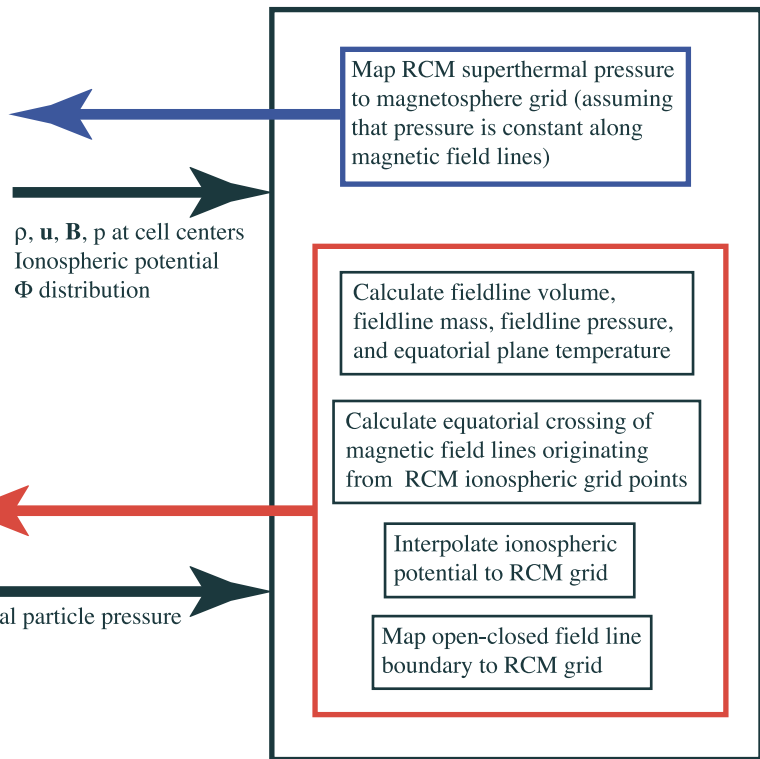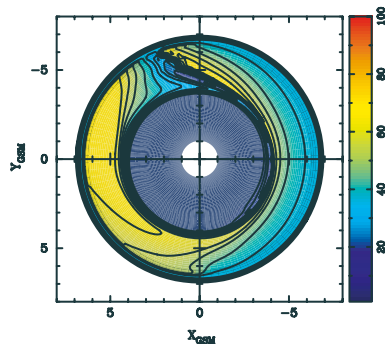
Global Magnetosphere–Ionosphere Model (MHD)

ρ, **u**, **B**, p at cell centers
Ionospheric potential
Φ distribution

Map RCM superthermal pressure to magnetosphere grid (assuming that pressure is constant along magnetic field lines)

Calculate fieldline volume, fieldline mass, fieldline pressure, and equatorial plane temperature

Calculate equatorial crossing of magnetic field lines originating from RCM ionospheric grid points

Interpolate ionospheric potential to RCM grid

Map open-closed field line boundary to RCM grid

Inner Magnetosphere Model (RCM)

Total particle pressure

Figure 1. Exchange of information between BATS-R-US (Block Adaptive Tree Solar-wind Roe-type Upwind Scheme) and RCM (Rice Convection Model) models.

[*Erickson et al.*, 1991], and coupling to the thermosphere [e.g., *Forbes and Harel*, 1989; *Wolf et al.*, 1986].

4. Coupling of Models

[18] The major scientific aim of this coupling of two numerical codes was to allow the MHD model to better represent the gradient/curvature drift physics in the inner magnetosphere and therefore to produce more realistic region-2 field-aligned currents. Technically, this is a challenging task, given the fact that the two models must be coupled in an overlapping three-dimensional region of the inner magnetosphere. Three-dimensional MHD solutions obtained on a computational grid that consists of self-similar cartesian blocks of varying resolution need to be translated to two-dimensional RCM quantities that are averages along magnetic fields lines anchored on a two-dimensional RCM ionospheric grid. A further complication is that both RCM and BATS-R-US contain an ionospheric module that returns two-dimensional electric field by solving either (A1) or (6) on different grids and with generally different models of ionospheric conductances.

[19] The most essential, and computationally difficult, part of the coupling process is 3-D to 2-D and inverse transformations that rely on tracing magnetic field lines. The coupling process implemented consists of running BATS-R-US with RCM being a module in the global MHD code and information being exchanged at regular intervals (Figure 1). Underlying this information exchange is tracing of magnetic fields lines. A novel way of computing these transformations implemented in the coupled code is described in Appendix B.

[20] As previously mentioned, the RCM is driven by several inputs that are typically estimated using statistical models. In this case, all these quantities will be provided through coupling with BATS-R-US. Conceptually, RCM solves equations (6) and (4) on the ionospheric polar grid. Both equations require knowledge of flux tube volume quantities $V = \int ds/B$ in the modeling region, which must contain only closed field lines. In the RCM, the grid extends from the pole to 9.86 degrees invariant magnetic latitude, but the outer (poleward) boundary of the modeling region is determined dynamically throughout a simulation and can be placed anywhere on the grid. Equation (6) is an elliptic partial differential equation and requires specification of the potential on the high-latitude boundary, which is taken from the MHD code. Ionospheric conductances used in (6) are the same ones used in the MHD ionospheric module. We note that in principle, it is not necessary in the coupled code for the RCM to solve (6), since the RCM can use the electrostatic potential calculated by the MHD ionospheric module. However, given the higher-resolution grid of the RCM in the inner magnetosphere, we implemented both options in the coupled code.

[21] Equation (4), in addition to the flux tube volume distribution, requires initial and boundary conditions for the plasma flux tube contents η. These are determined by taking MHD-computed ρ (mass density) and P (pressure) and

treating them as moments of the distribution function of an assumed shape (typically, a maxwellian or a kappa-shaped function) in the RCM. A set (typically, 150) of ηs representing both electrons and protons is thus computed everywhere in the RCM modeling region (for the initial condition at the beginning of the calculation) or only along the outer RCM boundary (as a boundary condition, throughout a simulation). We use the MHD temperature of the plasma sheet (which we take to be $kT = Pm_p/\rho$, where m_p is the proton mass) to set the temperature for the protons in the RCM to be $(7.8/8.8)kT$, and we set the electron temperature in the RCM to be $(1/8.8)kT$, in accordance with plasma sheet observations. Since it is possible that as the magnetic field inflates, the RCM outer boundary moves outward in the magnetosphere, and therefore the RCM modeling region acquires new grid points that do not have a solution, a mechanism is implemented to assign initial solutions to these newly acquired points by the same conversion as for the initial conditions.

[22] In the coupling framework (Figure 1), the MHD code (upper left box) typically is run for a short time (we have experimented with times from 10 s to 10 min), followed by the field line tracing module. Field line tracing is done globally (see below), and it returns either field line integrated quantities on the RCM grid points that anchor closed field lines or an indicator that field lines are open. In the same module, interpolations are performed, as necessary for transforming from the MHD grid to the RCM grid. Using results from the field line tracing, MHD-to-RCM conversions described above are performed, and a high-latitude RCM boundary location is determined. These calculations are depicted by the upper black arrow and the red composite box on the right side of Figure 1. The RCM (lower left box of Figure 1) is then run for the same time interval. The particle pressure obtained by the RCM is integrated over the distribution function (lower left-to-right black arrow on Figure 1) and is sent back to the MHD. Using results of the field-line tracing, pressure in the MHD code is corrected by the RCM solutions, assuming that RCM pressure is constant along magnetic field lines (blue right-to-left arrow of Figure 1). This loop is then repeated as long as necessary during a simulation. The optimal coupling frequency is a balance between the increasing time to couple more often and the minimal neccessary coupling for the models to drive each other, which depends on the event being simulated.

5. Initial Results

5.1. Input Conditions and Run Setup

[23] The run results described below were carried out under idealized conditions. The Earth's dipole was assumed to be perpendicular to the solar wind velocity and also parallel to the rotation axis; thus GSM and SM coordinates are identical for this simulation. The solar wind conditions were held constant with a density of 5 cm^{-3}, velocity of 400 km/s, and Mach number of 8 throughout the run. The interplanetary magnetic field (IMF) was held constant at 5 nT south for 8 hours and then sharply flipped to 5 nT north for another 8 hours. The temperature resulting from these conditions was 181,712 K, or 15.66 eV. First a steady state result was obtained without coupling to the RCM. Results

of this initial calculation were also used as an indication of the solutions that the MHD alone would produce for the same conditions. Then the full 16-hour, time-accurate, fully coupled run was completed and will be described below. For simplicity and to better understand initial results, in this first calculation, uniform ionospheric conductances (field-line integrated conductivities) were assumed with 4 S per hemisphere for the Pedersen conductance and 0 for Hall term. The ionospheric module in the MHD code was used to solve for the electric field and field-aligned currents, and the corresponding RCM module was not used, although RCM still calculated its own field-aligned currents and recorded them for comparison purposes.

5.2. Results for Steady Southward IMF

[24] The first part of the calculation, with the coupled code run for 8 hours under steady solar wind conditions, shows the effects of code coupling on the inner magnetospheric pressure, field-aligned currents, and the overall magnetic field configuration. As was mentioned before, in the coupled code, both MHD and RCM record physical quantities such as pressure, electrostatic potential, field-aligned currents, etc., at regular time intervals. There are advantages in looking at essentially the same quantities recorded by both models: first, some errors are introduced in translating RCM-computed quantities onto the MHD grid and vice versa due to interpolation; second, the different grid resolutions add to the errors independent of the interpolation algorithms.

5.2.1. Particle Pressure and Magnetic Field

[25] Figure 2 shows a comparison of pressures on the logarithmic scale ($LOG_{10}(P)$, where P is in nPa) in the magnetospheric equatorial plane, computed in two different ways for three different times (0, 4, and 8 hours) in a period of steady southward IMF. The upper left panel is a plot of the MHD pressure that would result in the absence of the RCM coupling. Owing to the inclusion of gradient/curvature drifts and adiabatic particle transport in the RCM in the inner magnetosphere, the pressures in the region $L < 10\ R_E$ are substantially higher than those computed with MHD alone. Both pressures are displayed on the RCM grid mapped from the ionosphere to the equatorial plane. Note that the RCM pressure is not set beyond the RCM modeling region, which can be seen by deep blue color outside the region roughly 10 R_E in size. The MHD pressures, on the other hand, are displayed on all closed field lines.

[26] Before coupling, the peak pressure in the MHD code is close to 1 nPa on the nightside. After running the coupled code for 8 hours, the pressure in the MHD code reaches peak values of 15 nPa, and in the RCM the peak pressure exceeds 18 nPa. One reason that there is a modest difference between the two columns of Figure 2 is that the MHD pressures are gradually nudged toward the RCM values but are never forced into instantaneous agreement to avoid potential numerical instabilities; another reason is that the numerical diffusion is greater and the grid resolution is lower in the MHD code so that the MHD pressure is smoother. The inner edge of the plasma sheet pressure is a bit closer to Earth in the MHD distribution than in the RCM, again because of numerical diffusion. The MHD-computed inner magnetospheric pressures affect the RCM-computed particle populations in two ways: (1) through their effect on the
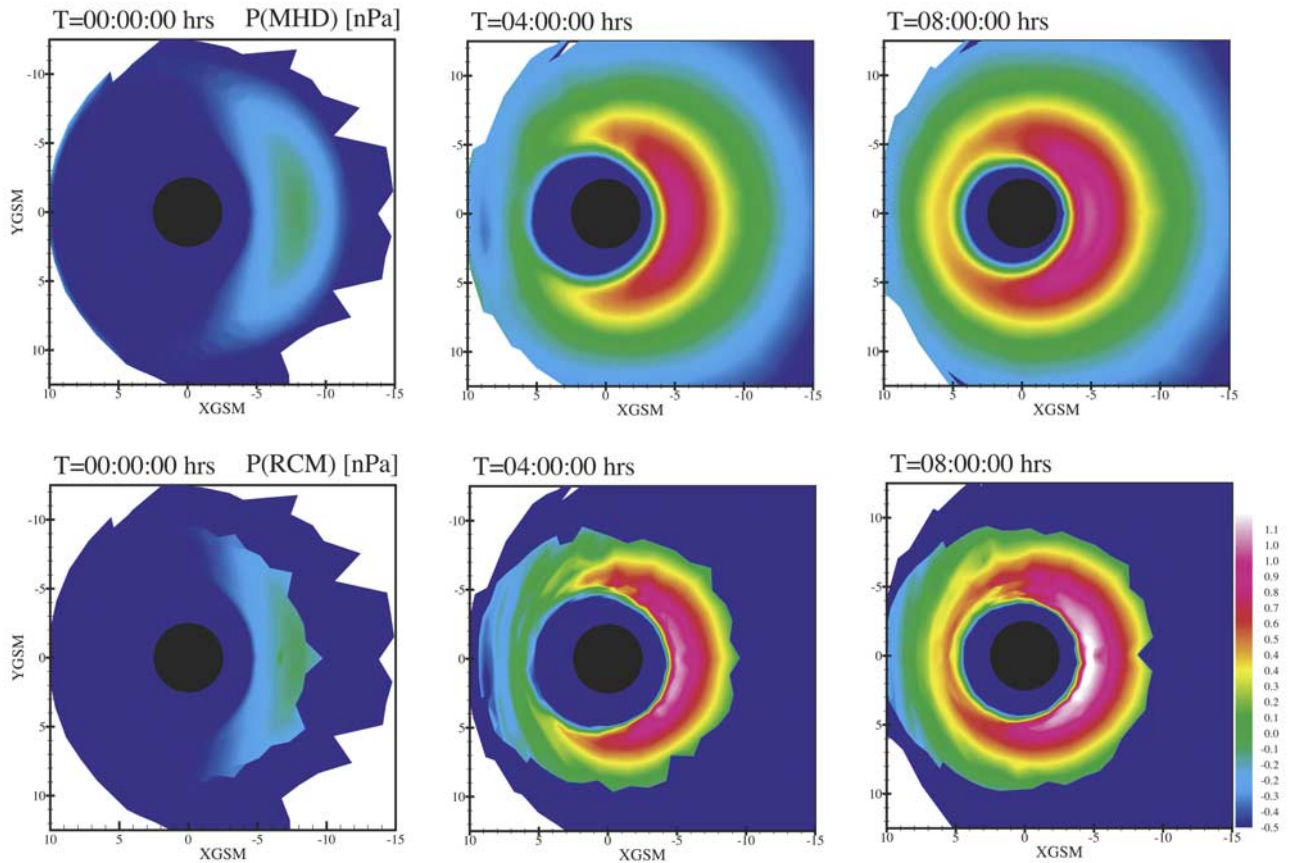
Figure 2. Comparisons of LOG_{10} of plasma pressures computed with the coupled code at 0, 4, and 8 hours during a long period with interplanetary magnetic field (IMF) $B_z = -5$ nT. (top) Pressure computed by BATS-R-US for coupled run. (bottom) RCM pressure for coupled run; both are plotted on the RCM grid mapped to the equatorial plane. Top left panel $T = 0$ also represents the noncoupled result or the instant before the coupling begins.

magnetic field and (2) through their indirect effect on the MHD-computed Birkeland currents and ionospheric potential. The differences in the pressure in the MHD code for the cases of coupling with the RCM and no coupling are made more quantitative in Figure 3, which shows a line plot of MHD pressures for the two runs along the negative X-axis.

[27] The dramatic effect that the buildup of the inner magnetospheric pressure has on the magnetic field solutions in the MHD code can be clearly seen in Figure 4, which shows MHD-computed pressures displayed in false colors on the linear scale in the $Y = 0$ plane. Superimposed are approximate magnetic field lines in white colors. Before coupling (upper panel $T = 0$), the characteristic region on the nightside where closed field lines meet those with both ends connected to the interplanetary magnetic field in the tail lobes (resembling an "X-line") is located at 12 R_E. With the RCM coupled (right panel), the particle pressure built up in the inner magnetosphere causes overall inflation of the magnetic field, with the interconnection region moving well beyond 30 R_E in the magnetotail.

[28] The inner-magnetospheric pressure distribution shows a strong day-night asymmetry, with average pressures on the nightside exceeding those on the dayside. That characteristic was pointed out in early RCM runs by *Wolf*

[1974] and has been a feature of essentially all runs since then. The same qualitative tendency exists in the observed particle pressure [e.g., *De Michelis et al.*, 1999]. There is a corresponding asymmetry in the cross-field currents, with
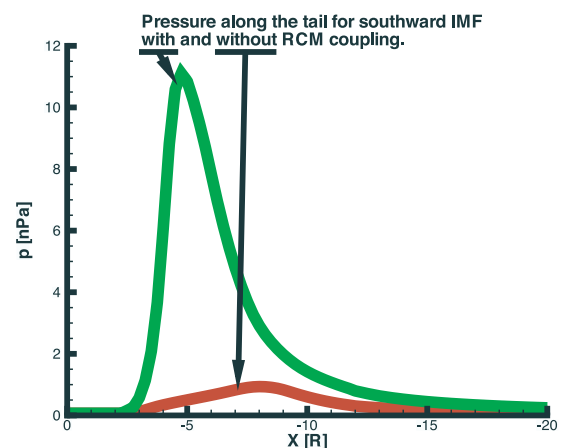

Figure 3. Comparison of MHD pressure computed along the tail axis using the MHD code with and without coupling to the RCM, for $t = 8$ hours.
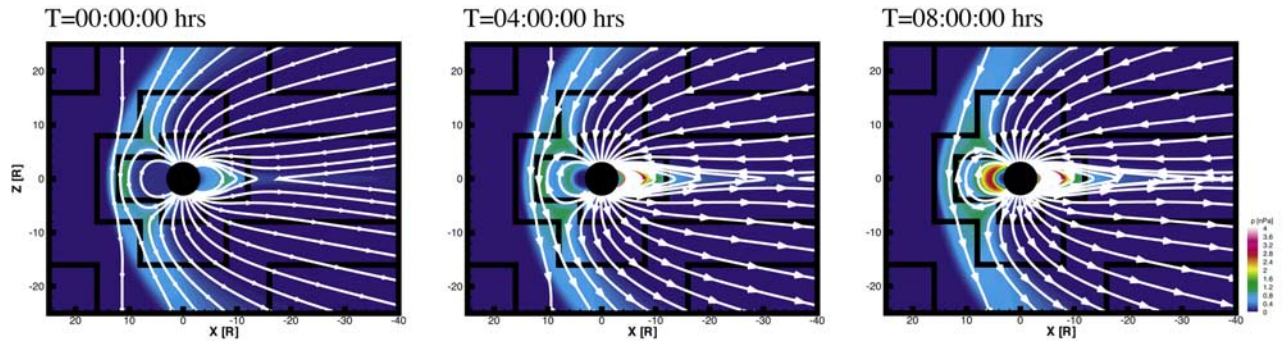
Figure 4. MHD pressure for 0, 4, and 8 hours during IMF $B_z = -5$ nT, color-coded on the linear scale in the noon-midnight plane. White lines are approximate magnetic field lines (B_y is very small). Black lines delineate grid block boundaries. Color scale saturates beyond 4 nPa. Time $T = 0$ also represents the noncoupled result or the instant before the coupling begins.

more westward ring current passing midnight than noon [e.g., *De Michelis et al.*, 1999].

[29] Figure 2 shows only a modest dawn-dusk pressure asymmetry. That asymmetry has been a matter of controversy recently. Whereas statistical analysis of in situ spacecraft measurements [*Lui*, 2003] indicate that the pressure peak is well before midnight in active times, energetic neutral atom images indicate that it is frequently past midnight in the main phase [*Brandt et al.*, 2002]. Some runs with the Comprehensive Ring Current Model have also showed peaks past midnight [*Fok et al.*, 2003]. The present runs, as exemplified by Figure 2, cannot contribute to resolving the controversy because (1) they assume uniform ionospheric conductance, and *Fok et al.* [2003] have argued that conductance gradients significantly affect the location of the ring current peak; (2) in

the run shown in Figure 2, the high-energy tail of the plasma-sheet-ion energy distribution was artificially truncated; the highest-energy channel for the run was $\lambda = 3995$ eV $(R_E/nT)^{2/3}$, which corresponds to about 25 keV at $L = 6.6$.

[30] Figure 5 compares the RCM-computed distribution functions for ions with $\lambda = 3995$ and 270 eV $(R_E/nT)^{2/3}$, corresponding to about 25 and 1.6 keV at synchronous orbit. Superimposed on the color plots of the flux tube content η (logarithmic scale) are contours of constant "effective potential"

$$\Phi_{eff} = \Phi + \Phi_c + \frac{\lambda_s}{q_s} V^{-2/3}, \qquad (8)$$

which are, according to equation (4), instantaneous flow paths for particles of a given λ. Note that the drift paths for
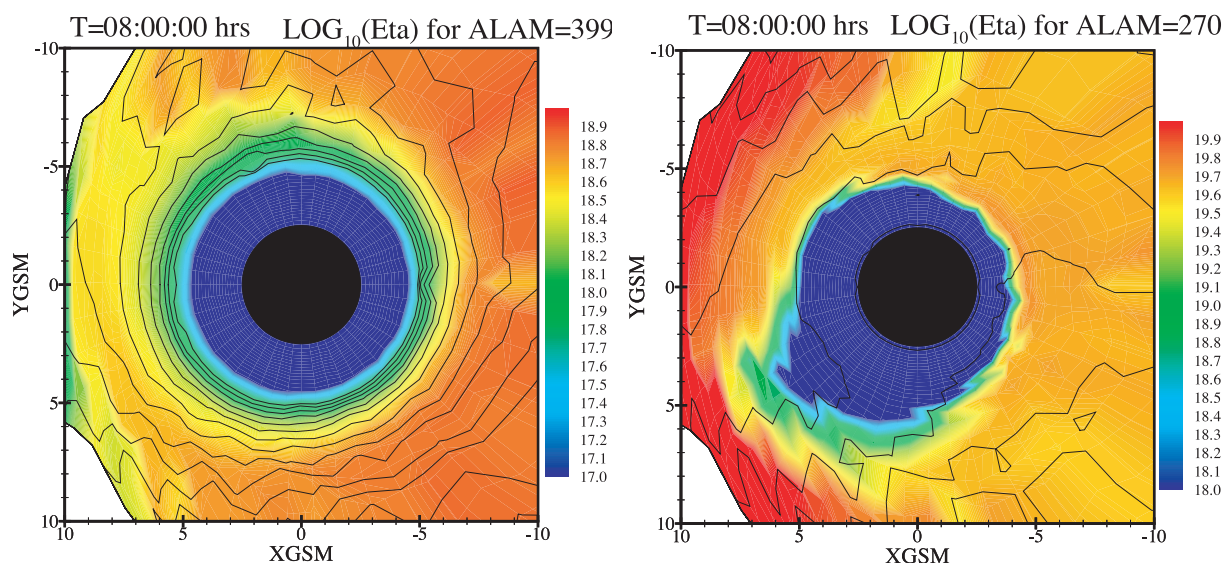

Figure 5. Plots of RCM flux tube content η at 0800 UT for particles with $\lambda = 3995$ (left) and $\lambda = 270$ (right), color-coded, in units of eV $(R_E/nT)^{2/3}$. Superimposed are contours of constant "effective potential" (see text), which are instantaneous flow lines.
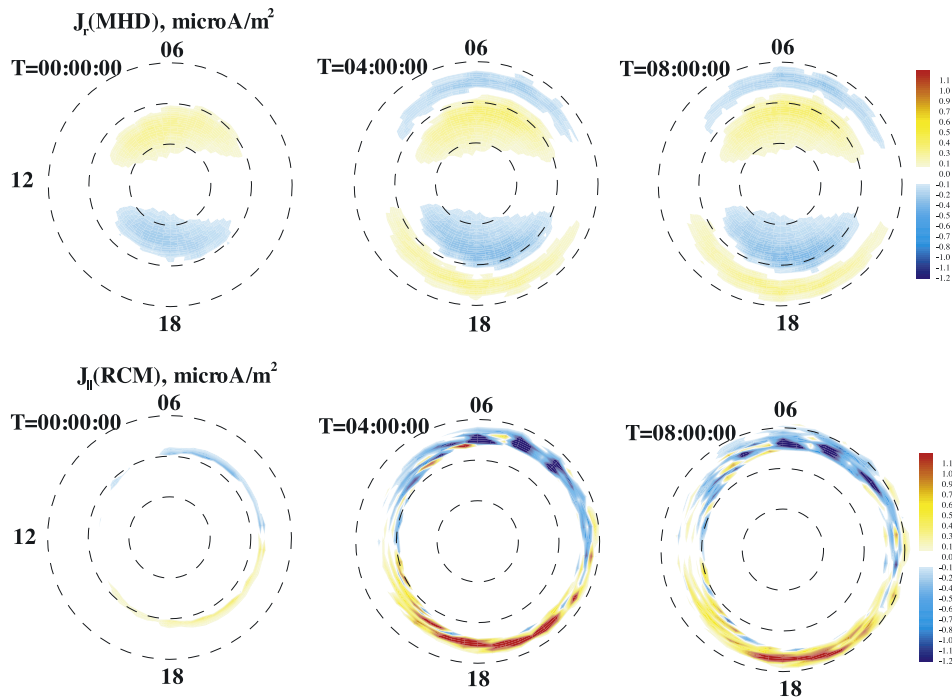
Figure 6. Birkeland currents for three times in a period of southward IMF, computed by the MHD (top) and RCM (bottom), for the Northern Hemisphere. Red (positive) is down into and blue (negative) is up from the ionosphere. In the bottom row, only currents computed by the RCM in its modeling region (region-2 currents) are shown, while the MHD-computed currents are global (both region-2 and region-1 systems.) In the calculation, only MHD currents were used.

λ = 3995 ions curve toward the duskside the Earth, as expected.

5.2.2. Field-Aligned Currents and Electric Fields

[31] Figure 6 shows Birkeland current displayed in a format similar to Figure 2. The RCM-computed currents (bottom row of Figure 6) are shown only in the RCM modeling region and are region-2 currents. They were not used in the calculation. The MHD-computed currents display initially ($T = 0$) mostly the region-1 system, with only traces of region-2 currents due to the above-mentioned lack of inner magnetospheric pressure (in the inner magnetosphere, field-aligned currents are related to pressure gradients through equation (5).) It is clear that the region-2 current (up from Earth on the dawnside and down to Earth on the duskside) is much stronger in the coupled code than in pure MHD. The RCM values (second column) were computed from the Vasyliunas equation using the MHD magnetic field and RCM pressures. The MHD values were computed by taking the field-aligned component of $\vec{\nabla} \times \vec{B}$ on a sphere of radius 3.5 R_E and mapping to ionospheric altitude to estimate the field-aligned current into the ionosphere.

[32] Note that the RCM-computed currents are stronger and sharper. One reason for this is that the equatorial currents in the RCM are mapped perfectly to the ionosphere, while in the MHD code, the currents are self-consistently driven down to the inner boundary, where they are mapped to the ionosphere. In order for the field-aligned currents generated near the equator to get to the body, the grid resolution must scale as the magnetic field.

If it does not (which is the case here), some field-aligned currents will diffuse off the field lines. Improved resolution near the body would both sharpen and strengthen the field-aligned currents.

[33] Figure 7 shows MHD-computed convection equipotentials in the ionospheric (corotating) frame for three times in the period of southward IMF, with superimposed MHD-computed field-aligned currents. Initially, equipotentials extend to subauroral latitudes. However, formation of region-2 currents at 4 hours results in shielding of lower (subauroral) latitudes from the full strength of the sunward convection. As can be seen, the region equatorward of the region-2 currents becomes significantly shielded by 8 hours.

5.2.3. Polar Cap Potential Drop

[34] Figure 8 shows the total northern polar cap potential drop computed by the coupled code in the course of 8 hours. In calculating Figure 8, we defined the polar cap potential as the difference between the maximum and minimum potentials in the entire Northern Hemisphere pattern. The initial value for the potential drop, 69 kV, is for the pure MHD simulation. However, the MHD simulation has not quite reached its steady state, and the potential in the MHD simulation increases to a constant value of 80 kV when run longer. This 80 kV potential drop is what the pure MHD code predicts for the chosen IMF and ionospheric parameters. After 8 hours of running the coupled code, the potential drop reaches 74 kV, an 8% deficit from the pure MHD result. This trend is in agreement with *Siscoe et al.* [2002], who predicted that the polar cap potential would be significantly decreased by the inclusion of realistic region-2
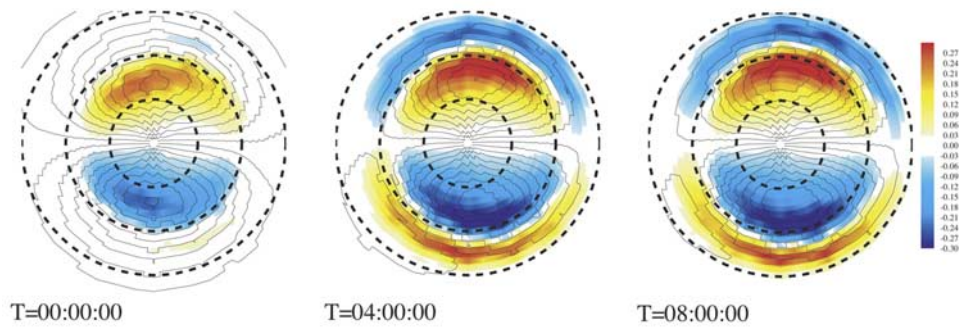
Figure 7. Ionospheric equipotentials (black lines) computed for three times in the period of southward IMF. The corotation electric field is not included in the plot. Contour step is 4 kV. Birkeland currents are also shown as color-coded plots. Dashed circles are drawn at 60, 70, and 80 degrees magnetic latitude.

Birkeland currents, which increase the effective ionospheric Pedersen conductance.

5.3. Response to a Northward Turning of the IMF

[35] At 0800 UT in the simulation, the IMF was suddenly turned to 5 nT north to analyze the response of the magnetosphere to an idealized change in the IMF conditions for the coupled MHD-RCM code. Figure 9 shows pressures computed by the coupled code at 0800 UT and then subsequently at 0820, 0830, 0840, 0850, and 0900 UT. Pressures were computed by the MHD code and are displayed in the equatorial plane. The color scale saturates at the maximum value of 4 nPa. As discussed in the previous section, at 0800 UT, there is a well-formed partial ring current characteristic of inner magnetospheric convection for southward IMF conditions. As the IMF B_z turned northward, Figure 9 shows how the magnetopause moves out in response. This is the expected response, the opposite of the erosion that occurs in response to a southward turning. Note also that the ring current becomes more and more symmetric owing to the fact that drift trajectories for the particles near the inner edge of the plasma sheet that were previously open now become closed. This is also an expected response; it has been recently observed by the HENA instrument on IMAGE spacecraft.

[36] Figure 10 shows the response of the inner magnetospheric potential distribution over the same 1-hour time period. The potential is shown in the rotating ionospheric frame for nine times between 0800 and 0920 UT. Equipotentials are spaced at 1 kV and they are color-coded with the values according to the color legend on the right side of the figure. Equipotentials with absolute values larger than 27 kV are not shown to emphasize the subauroral features. Note that the potential at 0810 UT is about the same as at 0800 UT. The northward turning of the IMF has had no effect, probably due to the time for the change to be advected from the sunward boundary of the calculation to the nose of the magnetosphere. Overshielding, characterized by a dusk-dawn electric field across much of the magnetosphere, is evident from 0820 to 0910. This can be seen as formation of secondary potential "vortices" on the duskside and dawnside equatorward of the region of antisunward flow.

[37] Overshielding was originally discovered and interpreted by *Kelley et al.* [1979] in observations by the Jicamarca incoherent backscatter radar. It has been extensively studied observationally by B. G. Fejer and collaborators [e.g., *Scherliess and Fejer*, 1997] and also theoretically using the RCM [*Spiro et al.*, 1988; *Fejer et al.*, 1990]. However, the results presented in Figure 10 represent the first full computer simulation of the overshielding effect, including both the inner magnetospheric electrodynamics and the solar wind/magnetosphere coupling.

[38] *Kelley et al.* [1979] originally associated the overshielding phenomenon with a reduction in the potential drop.
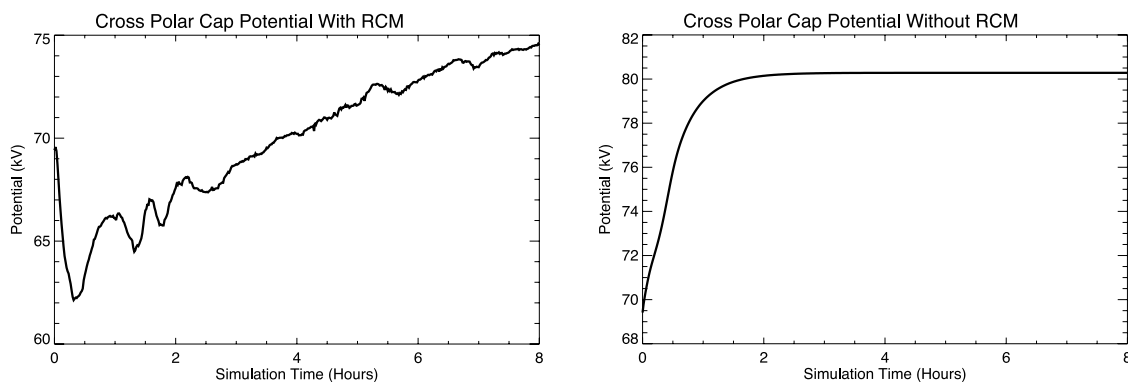

Figure 8. Polar cap potential drop versus time for the southward IMF period, for the coupled-code run (left) and the non-coupled-code run (right). The non-coupled-code run reaches steady state within an hour at about an 80 kV potential.
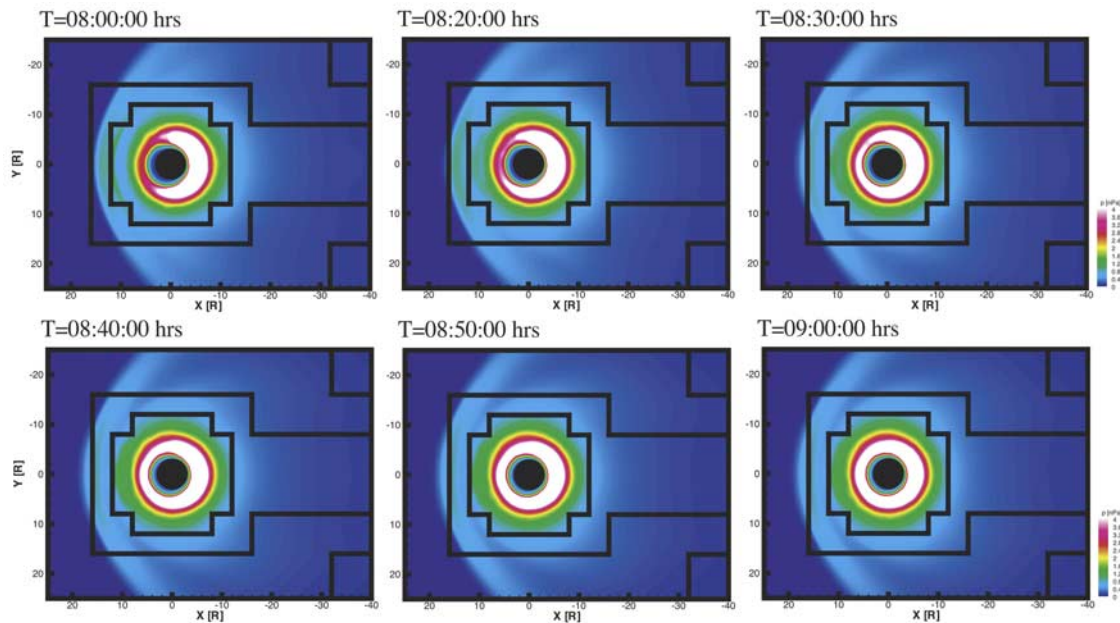
Figure 9. Changes in the equatorial pressure distribution in response to the northward turning of the IMF at 0800 UT for six times. To better show the global pressure distribution, the color scale saturates at 4 nPa; the peak values are higher.

However, RCM computer experiments in which the polar cap potential was suddenly decreased but the magnetic field configuration was kept constant in time produced over-shielding that was of quite short duration, too short to be consistent with the observed duration (typically 1–2 hours) [*Spiro et al.*, 1988]. *Fejer et al.* [1990] suggested that the magnetic reconfiguration of the magnetosphere due to a northward turning and the associated shrinkage of the polar
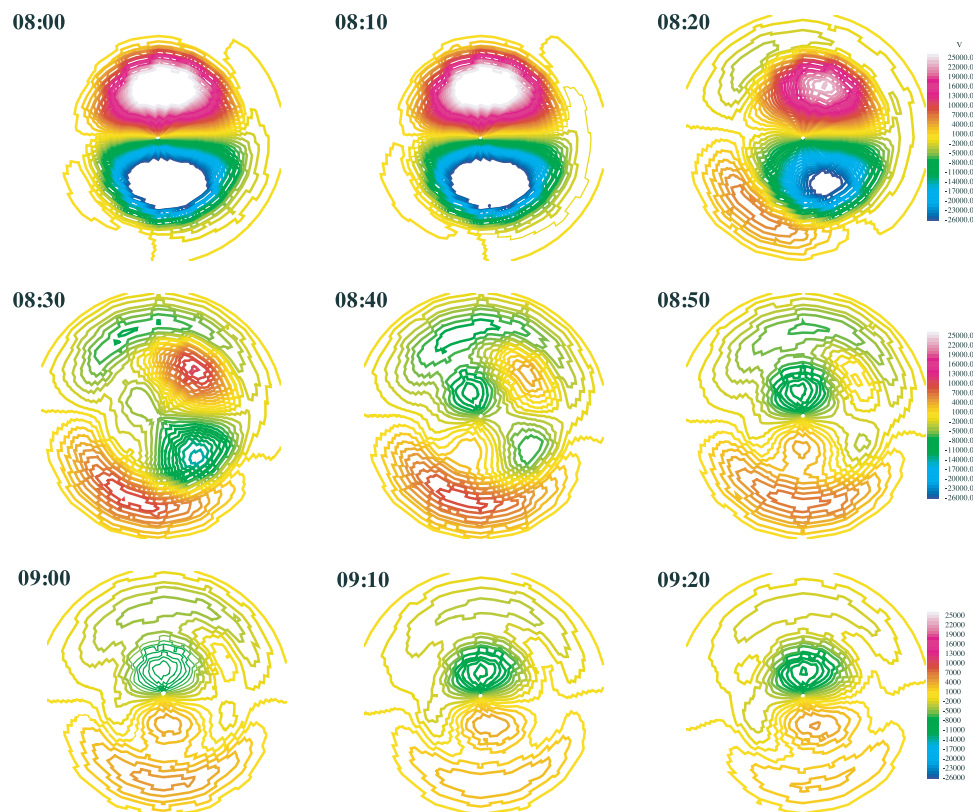

Figure 10. Ionospheric equipotentials after the northward turning of the IMF at 0800. Equipotential spacing is 1 kV. Contours with absolute values >27 kV are not shown.
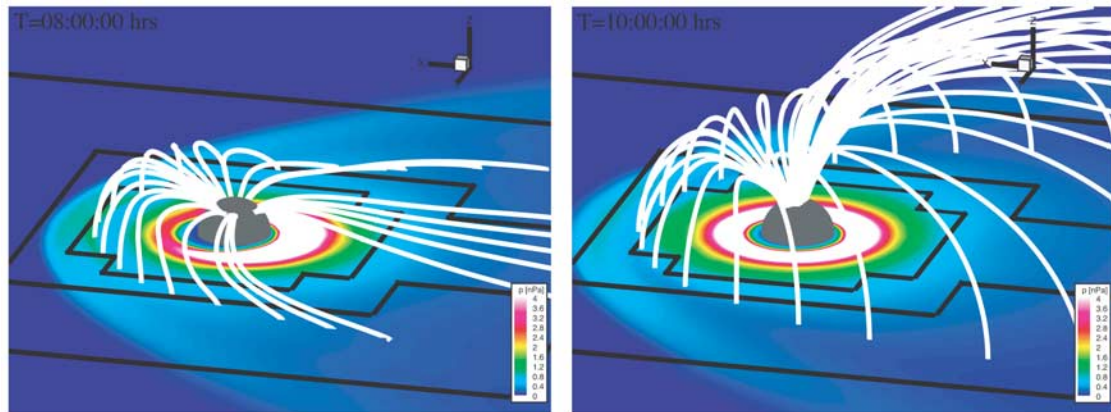
Figure 11. Last closed field lines just before northward turning and 2 hours after. The colors show the equatorial pressure distribution.

cap, also play a role in overshielding. Figure 11 illustrates the degree of magnetic reconfiguration that occurs when the IMF turns north. *Sazykin* [2000] confirmed the effect of magnetic reconfiguration on overshielding using RCM runs with time-dependent Hilmer-Voigt [*Hilmer and Voigt*, 1995] semiempirical magnetic field models. However, the present run is the first self-consistent theoretical calculation of the response of the inner magnetospheric electric field to a northward turning of the IMF. It is encouraging that it indicates overshielding with a duration that is comparable to the observations. Of course, detailed quantitative comparisons of coupled code simulations with observations of overshielding await coupled code simulations with a realistic ionospheric conductance distribution.

6. Summary

[39] We have presented a first report on the successful coupling of the Rice Convection Model of Earth's inner magnetosphere to the BATS-R-US global MHD model. The method of coupling has been described, including an innovative and efficient approach to tracing magnetic field lines.

[40] Run for steady southward IMF, the coupled code exhibits the classic characteristics of inner magnetospheric electrodynamics, including the formation of strong region-2 Birkeland currents that shield the inner magnetosphere from the dawn-dusk convection electric field. Inner magnetospheric particle pressures are much higher when computed with the coupled code than with the MHD code running alone. In response to the pressure increase, the MHD code predicts much more inflated magnetic field in the inner and central plasma sheet region.

[41] Beyond demonstrating consistency with established characteristics, we have also applied the coupled code to an issue that has not been computationally accessible before. Namely, the coupled code was run through a sudden northward turning of the IMF from $Bz = -5$ nT to +5 nT. The inner magnetospheric electric field temporarily exhibited an overshielding (dusk to dawn) electric field, which is a well-established observational and theoretical feature. However, the coupled code can also address an interesting question related to the time response that could not be attacked computationally before. The subauroral ionospheric electric field begins to respond to the northward turning quickly,

about 10 min after the northward IMF reaches the dayside magnetopause. The overshielding effect peaks about 20 min later and lasts just over an hour. These timescales involve the physics of both the outer and inner magnetosphere. We are therefore making a tentative prediction that can be checked against observations. These new physical conclusions concerning the polar cap potential and the time delay involved in the inner magnetospheric response to northward turning are tentative because they are based on runs carried out for a uniform conductance ionosphere.

Appendix A: BATS-R-US Overview

[42] BATS-R-US solves the MHD equations with a finite volume discretization using the conservative variables: density ρ, momentum density $\rho\mathbf{u}$, magnetic field $\mathbf{B}$, and the total energy density e which is the sum of the thermal, kinetic, and magnetic energy densities. Using the conservative variables is necessary to obtain correct jump conditions across shock waves, e.g., the bow shock. Away from the shock it may be advantageous to use the nonconservative equations. In BATS-R-US there is an option of using the pressure equation (last line of equation (1)) instead of the energy conservation equation near the Earth inside the bow shock, which results in a more robust numerical scheme.

[43] The MHD equations also contain the constraint that $\nabla \cdot \mathbf{B} = 0$. Enforcing this constraint numerically, particularly in shock-capturing codes, can be done in a number of ways [see *Tóth*, 2000, and references therein]. In BATS-R-US, four types of divergence control schemes are implemented: the eight-wave scheme [*Powell*, 1994; *Powell et al.*, 1995], the diffusive/parabolic approach [*Dedner et al.*, 2003], the projection scheme [*Brackbill and Barnes*, 1980], and a conservative form of the constrained transport scheme extended to adaptive grids [*Tóth and Roe*, 1996]. For magnetospheric applications all these schemes produce very similar results, but there are differences in efficiency and robustness. In the calculations presented in this paper the most efficient and robust eight-wave scheme is used.

[44] In the eight-wave scheme the MHD equations are written in a symmetrizable form [*Godunov*, 1972] which contains extra terms proportional to $\nabla \cdot \mathbf{B} = 0$. This equation leads to eight eigenvalue/eigenvector pairs: an entropy wave,

two Alfvén waves, two magnetofast waves, two magneto-slow waves, and an eighth eigenvalue/eigenvector pair associated with the jump of the normal component of the magnetic field. The eight-wave scheme advects the errors associated with the divergence of the magnetic field and thus keeps the error at the truncation level. The expressions and scaling of the eigenvectors are more intricate than in gasdynamics [*Roe and Balsara*, 1996].

[45] Adaptive mesh refinement (AMR) techniques [e.g., *Berger and Colella*, 1989; *Quirk*, 1991] that automatically adapt the computational grid to the solution of the governing PDEs can be very effective in treating problems with disparate length scales. Methods of this type avoid under-resolving the solution in regions deemed of interest (e.g., high-gradient regions) and, conversely, avoid overresolving the solution in other less interesting regions (low-gradient regions), thereby saving orders of magnitude in computing resources for many problems.

[46] Keeping in mind the desire for high performance on massively parallel computer architectures, a relatively simple yet effective block-based AMR technique has been developed [*Stout et al.*, 1997]. The computational cells are embedded in regular structured blocks of equal sized cells. Typically, blocks consisting of anywhere between $4 \times 4 \times 4 = 64$ and $12 \times 12 \times 12 = 1728$ cells are used. Computational grids are composed of many self-similar blocks. Although each block within a grid has the same data storage requirements, blocks may be of different sizes in terms of the volume of physical space that they occupy. Starting with an initial mesh consisting of blocks of equal size (i.e., equal resolution), adaptation is accomplished by the dividing and coarsening of appropriate solution blocks. In regions requiring increased cell resolution, a "parent" block is refined by dividing itself into eight "children." Each of the eight octants of a parent block becomes a new block having the same number of cells as the parent and thereby doubling the cell resolution in the region of interest. Conversely, in regions that are deemed overresolved, the refinement process is reversed, and eight children are coarsened and coalesced into a single parent block. In this way, the cell resolution is reduced by a factor of 2. Standard multigrid-type restriction and prolongation operators are used to evaluate the solution on all blocks created by the coarsening and division processes, respectively.

[47] In order that the update scheme for a given iteration or time step can be applied directly to all blocks in an independent manner, some additional solution information is shared between adjacent blocks having common interfaces. This information is stored in an additional two layers of overlapping "ghost cells" associated with each block. The block adaptation readily enables domain decomposition and effective load balancing and leads to low communication overhead between solution cells within the same block.

[48] As noted above, each level of refinement in the grid introduces cells that are smaller by a factor of 2 in each dimension from those one level higher in the grid. Typically, calculations may have 10–20 levels of refinement. In the case of 20 levels of refinement, the finest cells on the mesh are more than one million times (2^{20}) smaller in each dimension than the coarsest cells.

[49] The state of the magnetosphere is controlled by conditions in the solar wind and in the ionosphere. Solar wind conditions are imposed as boundary conditions at the upwind boundary of the simulation domain. These boundaries are put far enough away that they do not influence the solution.

[50] The ionosphere-magnetosphere (I-M) coupling, on the other hand, is a highly nonlinear two-way interaction which strongly affects the large-scale behavior of both domains [*Ridley et al.*, 2004]. Self-consistent global magnetosphere models include some kind of dynamic ionosphere model which interacts with the magnetosphere and provides ionospheric boundary conditions actively responding to changing magnetospheric conditions.

[51] While mass exchange between the ionosphere and the magnetosphere is undoubtedly of major importance, the dominant component of I-M coupling is a system of field-aligned currents (FACs) connecting the magnetosphere and the high-latitude ionosphere. These FACs carry momentum (electromagnetic stress) and energy (Poynting flux) along stretched magnetic field lines connecting the ionosphere and the magnetosphere. Self-consistent global magnetosphere models need to describe the generation and closure of these FACs through appropriate boundary conditions and embedded non-MHD models.

[52] BATS-R-US has been coupled to two ionosphere models to provide ionospheric current closure (the user can choose from the two available models) and a drift model to account for the generation and closure of FACs. The simplest I-M coupling procedure involves a height-integrated electrostatic ionosphere model. In this case the MHD code has an inner boundary at a radius of R_B (for explicit time-stepping we typically use $R_B = 2.5 \ R_E$). At this inner boundary, the plasma density, temperature, and velocity are specified. In addition, the magnetic field is allowed to float (zero gradient of the normal component), so currents can flow along the boundary. The velocities which are imposed on the boundary are calculated in the ionosphere in a three step process [*Goodman*, 1995]:

[53] 1. Field-aligned currents are calculated from the curl of the magnetic field at $R_B + 1 \ R_E$, and these are mapped down to the ionosphere.

[54] 2. A height-integrated ionospheric conductance pattern is generated and the ionospheric potential is calculated from the equation:

$$j_R(R_E) = \left[\boldsymbol{\nabla}_\perp \cdot (\Sigma \cdot \nabla \psi)_\perp \right]_{R=R_E}, \tag{A1}$$

which describes the relationship between the height-integrated conductance tensor, Σ, the ionospheric potential, ψ, and the radial component of the current, j_R.

[55] 3. Finally, the electric potential is mapped out along field lines to the inner boundary at R_B where electric fields and velocities are generated. The corotation velocity field is added to the ionosphere generated velocity field.

[56] The details of our conductance model as well as some simulation results using this method are given by *Ridley et al.* [2001, 2002, 2004].

Appendix B: Ray Tracing

[57] In order to compute the necessary quantities to send to the RCM and in turn to use the RCM pressures back in

the MHD model, we need to accurately and efficiently trace magnetic field lines. Complicating this procedure is the fact that BATS-R-US is a massively parallel code that distributes different portions of the grid (blocks) to different processors. Assuming that all the magnetic field information were to reside on one processor, a "brute force" approach to trace each line would take a significant amount of time. However, since our magnetic field data is distributed across many processors in the adaptive block structure of the MHD model, a different and much more efficient method was designed for this coupled code.

[58] As described earlier, each processor contains many blocks of data, which together fill the simulation domain. Each block contains all that is necessary to advance the MHD solution in its region of space. Each block knows who its neighboring blocks are and how to exchange information with them, as they may reside on other processors. This exchange is handled through two shells of ghost cells which surround the block and are filled with neighboring block information. The ray tracer begins by tracing the magnetic field within each block, with a grid of points on the outer surface of the block storing the two end points of the magnetic field line which pass through that point. Each point on the block surface then knows the mapping of that small subset of field lines. The next step is a recursive exchange of information between neighboring blocks and their shared faces. Tracing information is matched up at the faces such that both blocks sharing the face now know the tracing information of magnetic field lines in a larger volume. This iterative process continues until there are no changes to any tracing information, in which case the information about magnetic field tracing has propagated throughout the domain. Traces that have both ends on the ionosphere are then deemed to be closed field lines and will be considered for coupling to the RCM. Each cell now only needs to trace to the outer edge of its block and interpolate to determine the exact latitude and longitude mapping of its magnetic field line.

[59] This parallel tracing method is several orders of magnitude faster than a serial "brute force" approach, and efficiency improves with more processors and blocks. Conceptually, the numerical algorithm is equivalent to solving a large system of linear equations and is bound to converge to the solution. In practice, however, we have to distinguish between different types of magnetic field lines (e.g., open, closed and anchored to the ionosphere, loops). When implemented in the computer code, these different "clauses" introduce nonlinearity, and convergence is not guaranteed. While we have not performed a rigorous mathematical analysis of the algorithm, our experience and testing showed that convergence is always achieved and to the right solution in the closed field line region.

[60] This tracing procedure can have any number of uses, but coupling to the RCM requires that we integrate magnetic field volumes as well as average field pressures and densities. In order to compute these terms, we simply compute the fraction of the field volume that exists in each block for each latitude/longitude pair desired and a parallel global sum of these pieces. When the RCM is ready to provide a pressure back to the MHD model, each cell already knows where it maps to from the ray tracing and can easily interpolate its RCM pressure.

References

Berger, M. J., and P. Colella (1989), Local adaptive mesh refinement for shock hydrodynamics, *J. Comput. Phys.*, *82*, 67–84.

Blanc, M., and A. D. Richmond (1980), The ionospheric disturbance dynamo, *J. Geophys. Res.*, *85*, 1669–1686.

Brackbill, J., and D. Barnes (1980), The effect of nonzero $\nabla \cdot \mathbf{B}$ on the numerical solution of the magnetohydrodynamic equations, *J. Comput. Phys.*, *35*, 426–430.

Brandt, P. C., S. Ohtani, D. G. Mitchell, M.-C. Fok, E. C. Roelof, and R. Demajistre (2002), Global ENA observations of the storm main-phase ring current: Implications for skewed electric fields in the inner magnetosphere, *Geophys. Res. Lett.*, *29*(20), 1954, doi:10.1029/2002GL015160.

Chen, M. W., L. R. Lyons, and M. Schulz (2000), Stormtime ring current formation: A comparison between single- and double-dip model storms with similar transport characteristics, *J. Geophys. Res.*, *105*, 27,755–27,765.

Dedner, A., F. Kemm, D. Kröner, C. Munz, T. Schnitzer, and M. Wesenberg (2003), Hyperbolic divergence cleaning for the MHD equations, *J. Comput. Phys.*, *175*, 645–673.

Delamere, P. A., D. W. Swift, and H. C. Stenbaek-Nielsen (2001), An explanation of the ion cloud morphology in the CRRES plasma injection experiments, *J. Geophys. Res.*, *106*, 21,289–21,295.

De Michelis, P., I. A. Daglis, and G. Consolini (1999), An average image of proton plasma pressure and of current systems in the equatorial plane derived from ampte/cce-chem measurements, *J. Geophys. Res.*, *104*, 28,615–28,624.

De Zeeuw, D. L., T. I. Gombosi, C. P. T. Groth, K. G. Powell, and Q. F. Stout (2000), An adaptive MHD method for global space weather simulations, *IEEE Trans. Plasma Sci.*, *28*, 1956–1965.

Erickson, G. M., R. W. Spiro, and R. A. Wolf (1991), The physics of the Harang discontinuity, *J. Geophys. Res.*, *96*, 1633–1645.

Fejer, B. G., R. W. Spiro, R. A. Wolf, and J. C. Foster (1990), Latitudinal variation of perturbation electric fields during magnetically disturbed periods: 1986 SUNDIAL observations and model results, *Ann. Geophys.*, *8*, 441–454.

Fok, M., T. E. Moore, and D. C. Delcourt (1999), Modeling of inner plasma sheet and ring current during substorms, *J. Geophys. Res.*, *104*(A7), 14,557–14,569.

Fok, M., R. A. Wolf, R. W. Spiro, and T. E. Moore (2001), Comprehensive computational model of Earth's ring current, *J. Geophys. Res.*, *106*(A5), 8417–8424.

Fok, M., et al. (2003), Global ENA IMAGE simulations, *Space Sci. Rev.*, *109*, 77–103.

Forbes, J. M., and M. Harel (1989), Magnetosphere-thermosphere coupling: An experiment in interactive modeling, *J. Geophys. Res.*, *94*, 2631–2644.

Garner, T. W. (2003), Numerical experiments on the inner magnetospheric electric field, *J. Geophys. Res.*, *108*(A10), 1373, doi:10.1029/2003JA010039.

Godunov, S. K. (1972), Symmetric form of the equations of magneto-hydrodynamics (in Russian), in *Numerical Methods for Mechanics of Continuum Medium*, vol. 1, pp. 26–34, Siberian Branch of USSR Acad. of Sci., Novosibirsk.

Goodman, M. L. (1995), A three-dimensional, iterative, mapping procedure for the implemenation of an ionosphere-magnetosphere anisotropic Ohm's law boundary condition in global magnetohydrodynamic simulations, *Ann. Geophys.*, *13*, 843–853.

Harel, M., R. A. Wolf, P. H. Reiff, R. W. Spiro, W. J. Burke, F. J. Rich, and M. Smiddy (1981a), Quantitative simulation of a magnetospheric substorm: 1. Model logic and overview, *J. Geophys. Res.*, *86*, 2217–2241.

Harel, M., R. A. Wolf, R. W. Spiro, P. H. Reiff, C. Chen, W. J. Burke, F. J. Rich, and M. Smiddy (1981b), Quantitative simulation of a magnetospheric substorm: 2. Comparison with observations, *J. Geophys. Res.*, *86*, 2242–2260.

Hilmer, R. V., and G. Voigt (1995), A magnetospheric magnetic field model with flexible current systems driven by independent physical parameters, *J. Geophys. Res.*, *100*, 5613–5626.

Jaggi, R. K., and R. A. Wolf (1973), Self-consistent calculation of the motion of a sheet of ions in the magnetosphere, *J. Geophys. Res.*, *78*, 2852.

Janhunen, P. (1996), GUMICS-3: A global ionosphere-magnetosphere coupling simulation with high ionospheric resolution, in *Proceedings of the ESA 1996 Symposium on Environment Modelling for Space-Based Applications*, ESA SP-392, pp. 233–239, Eur. Space Agency, Paris.

Jordanova, V. K., L. M. Kistler, C. J. Farrugia, and R. B. Torbert (2001), Effects of inner magnetospheric convection on ring current dynamics: March 10–12, 1998, *J. Geophys. Res.*, *106*(A12), 29,705–29,720.

Kelley, M. C., B. G. Fejer, and C. A. Gonzales (1979), An explanation for anomalous ionospheric electric fields associated with a northward turning of the interplanetary magnetic field, *Geophys. Res. Lett.*, *6*, 301–304.

Liemohn, M. W., J. U. Kozyra, C. R. Clauer, G. V. Khazanov, and M. F. Thomsen (2002), Adiabatic energization in the ring current and its relation to other source and loss terms, *J. Geophys. Res.*, *107*(A4), 1045, doi:10.1029/2001JA000243.

Lui, A. (2003), Flux transfer events in global numerical simulations of the magnetosphere, *Geophys. Res. Lett.*, *30*(16), 1846, doi:10.1029/2003GL017596.

Lyon, J. G., J. Fedder, and J. Huba (1986), The effect of different resistivity models on magnetotail dynamics, *J. Geophys. Res.*, *91*, 8057–8064.

Nishikawa, K. (2001), Global particle simulation study of substorm onset and particle acceleration, *Space Sci. Rev.*, *95*(1-2), 361–371.

Ogino, T., and R. J. Walker (1984), A magnetohydrodynamic simulation of the bifurcation of tail lobes during intervals with a northward interplanetary magnetic field, *Geophys. Res. Lett.*, *11*, 1018–1021.

Peymirat, C., A. D. Richmond, and R. G. Roble (2002), Neutral wind influence on the electrodynamic coupling between the ionosphere and the magnetosphere, *J. Geophys. Res.*, *107*(A1), 1006, doi:10.1029/2001JA900106.

Powell, K. G. (1994), An approximate Riemann solver for magnetohydrodynamics (that works in more than one dimension), *Tech. Rep. 94-24*, Inst. for Comput. Appl. in Sci. and Eng., NASA Langley Space Flight Cent., Hampton, Va.

Powell, K. G., P. L. Roe, R. S. Myong, T. I. Gombosi, and D. L. De Zeeuw (1995), An upwind scheme for magnetohydrodynamics, in *Proceedings of AIAA 12th Computational Dynamics Conference*, AIAA-95-1704, p. 661, Am. Inst. of Aeron. and Astron., San Diego, Calif.

Powell, K. G., P. L. Roe, T. J. Linde, T. I. Gombosi, and D. L. De Zeeuw (1999), A solution-adaptive upwind scheme for ideal magnetohydrodynamics, *J. Comput. Phys.*, *154*(2), 284–309.

Quirk, J. J. (1991), An adaptive grid algorithm for computational shock hydrodynamics, Ph.D. thesis, Cranfield Inst. of Technol., Cranfield, U. K.

Raeder, J., R. J. Walker, and M. Ashour-Abdalla (1995), The structure of the distant geomagnetic tail during long periods of northward IMF, *Geophys. Res. Lett.*, *22*, 349–352.

Ridley, A. J., and M. W. Liemohn (2002), A model-derived storm time asymmetric ring current driven electric field description, *J. Geophys. Res.*, *107*(A8), 1151, doi:10.1029/2001JA000051.

Ridley, A. J., D. L. De Zeeuw, T. I. Gombosi, and K. G. Powell (2001), Using steady-state MHD results to predict the global state of the magnetosphere-ionosphere system, *J. Geophys. Res.*, *106*, 30,067–30,076.

Ridley, A. J., K. C. Hansen, G. Tóth, D. L. De Zueew, T. I. Gombosi, and K. G. Powell (2002), University of Michigan MHD results of the GGCM metrics challenge, *J. Geophys. Res.*, *107*(A10), 1290, doi:10.1029/2001JA000253.

Ridley, A. J., T. I. Gombosi, and D. I. De Zeeuw (2004), Ionosphere control of the magnetosphere: Conductance, *Ann. Geophys.*, *22*, 567–584.

Robinson, R., R. Vondrak, K. Miller, T. Dabbs, and D. Hardy (1987), On calculating ionospheric conductances from the flux and energy of precipitating electrons, *J. Geophys. Res.*, *92*, 2565–2569.

Roe, P. L., and D. S. Balsara (1996), Notes on the eigensystem of magnetohydrodynamics, *SIAM J. Appl. Math.*, *56*(1), 57–67.

Sazykin, S. Y. (2000), Theoretical studies of penetration of magnetospheric electric fields to the ionosphere, Ph.D. thesis, Utah State Univ., Logan, Utah.

Sazykin, S., R. A. Wolf, R. W. Spiro, T. I. Gombosi, D. L. De Zeeuw, and M. F. Thomsen (2002), Interchange instability in the inner magnetosphere associated with geosynchronous particle flux decreases, *Geophys. Res. Lett.*, *29*(10), 1448, doi:10.1029/2001GL014416. (Correction, *Geophys. Res. Lett.*, *29*(16), 1778, doi:10.1029/2002GL015846.)

Scherliess, L., and B. G. Fejer (1997), Storm time dependence of equatorial disturbance dynamo zonal electric fields, *J. Geophys. Res.*, *102*(A11), 24,037–24,046.

Siscoe, G. L. (1979), A Dst contribution to the equatorward shift of the aurora, *Planet. Space Sci.*, *27*, 997.

Siscoe, G. L., G. M. Erickson, B. U. Ö. Sonnerup, N. C. Maynard, J. A. Schoendorf, K. D. Siebert, D. R. Weimer, W. W. White, and G. R. Wilson (2002), Hill model of transpolar potential saturation: Comparisons with MHD simulations, *J. Geophys. Res.*, *107*(A6), 1075, doi:10.1029/2001JA000109.

Spiro, R. W., and R. A. Wolf (1984), Electrodynamics of convection in the inner magnetosphere, in *Magnetospheric Currents*, edited by T. A. Potemra, p. 247, AGU, Washington, D. C.

Spiro, R. W., M. Harel, R. A. Wolf, and P. H. Reiff (1981), Quantitative simulation of a magnetospheric substorm: 3. Plasmaspheric electric fields and evolution of the plasmapause, *J. Geophys. Res.*, *86*, 2261–2272.

Spiro, R. W., R. A. Wolf, and B. G. Fejer (1988), Penetration of high-latitude electric-field effects to low latitudes during SUNDIAL 1984, *Ann. Geophys.*, *6*, 39–50.

Stout, Q. F., D. L. De Zeeuw, T. I. Gombosi, C. P. T. Groth, H. G. Marshall, and K. G. Powell (1997), Adaptive blocks: A high-performance data structure, paper presented at Supercomputing 1997 Conference, IEEE Comput. Soc., San Jose, Calif.

Tanaka, T. (1995), Generation mechanisms for magnetosphere-ionosphere current systems deduced from a three-dimensional MHD simulation of the solar wind-magnetosphere-ionosphere coupling process, *J. Geophys. Res.*, *100*(A7), 12,057–12,074.

Toffoletto, F., J. Birn, M. Hesse, R. W. Spiro, and R. A. Wolf (2001), Modeling inner magnetospheric electrodynamics, in *Chapman Conference on Space Weather*, Geophys. Monogr. Ser., vol. 125, edited by P. Song, H. J. Singer, and G. L. Siscoe, pp. 265–272, AGU, Washington, D. C.

Toffoletto, F., S. Sazykin, R. Spiro, and R. Wolf (2003), Inner magnetospheric modeling with the Rice Convection Model, *Space Sci. Rev.*, *107*, 175–196.

Toffoletto, F. R., R. W. Spiro, R. A. Wolf, M. Hesse, and J. Birn (1996), Self-consistent modeling of inner magnetospheric convection, in *Proceedings of Third International Conference on Substorms (ICS-3)*, ESA SP-389, edited by E. J. Rolfe and B. Kaldeich, pp. 223–230, Eur. Space Agency, Paris.

Toffoletto, F. R., R. W. Spiro, R. A. Wolf, J. Birn, and M. Hesse (2000), Computer experiments on substorm growth and expansion, in *Proceedings of the 5th International Conference on Substorms*, ESA SP-443, edited by A. Wilson, pp. 351–355, Eur. Space Agency, Paris.

Tóth, G. (2000), The $\nabla \cdot \mathbf{B}$ constraint in shock capturing magnetohydrodynamic codes, *J. Comput. Phys.*, *161*, 605–652.

Tóth, G., and P. L. Roe (1996), Divergence- and curl-preserving prolongation and restriction formulae, *J. Comput. Phys.*, *180*, 736–750.

Vasyliunas, V. M. (1970), Mathematical models of magnetospheric convection and its coupling to the ionosphere, in *Particles and Fields in the Magnetosphere*, edited by B. M. McCormack, pp. 60–71, D. Reidel, Norwell, Mass.

White, W. W., G. L. Siscoe, G. M. Erickson, Z. Kaymaz, N. C. Maynard, K. D. Siebert, B. U. Ö. Sonnerup, and D. R. Weimer (1998), The magnetospheric sash and the cross-tail S, *Geophys. Res. Lett.*, *25*(10), 1605–1608.

Winglee, R. M. (1994), Non-MHD influences on the magnetospheric current system, *J. Geophys. Res.*, *99*, 13,437–13,454.

Wolf, R. (1974), Calculations of magnetospheric electric fields, in *Magnetospheric Physics*, edited by B. M. McCormac, pp. 167–177, D. Reidel, Norwell, Mass.

Wolf, R. A. (1983), The quasi-static (slow-flow) region of the magnetosphere, in *Solar Terrestrial Physics*, edited by R. L. Carovillano and J. M. Forbes, pp. 303–368, D. Reidel, Norwell, Mass.

Wolf, R. A., M. Harel, R. W. Spiro, G. Voigt, P. H. Reiff, and C. K. Chen (1982), Computer simulation of inner magnetospheric dynamics for the magnetic storm of July 29, 1977, *J. Geophys. Res.*, *87*, 5949–5962.

Wolf, R. A., G. A. Mantjoukis, and R. W. Spiro (1986), Theoretical comments on the nature of the plasmapause, *Adv. Space Res.*, *6*, 177–186.

————————

D. L. De Zeeuw, T. I. Gombosi, A. J. Ridley, and G. Tóth, Center for Space Environment Modeling, University of Michigan, 2455 Hayward Street, Ann Arbor, MI 48109, USA. (darrens@umich.edu)

S. Sazykin and R. A. Wolf, Department of Physics and Astronomy, MS-108, Rice University, 6100 South Main Street, Houston, TX 77005-1982, USA. (rawolf@rice.edu)